inorganics

MDPI

Article

AgCl-ZnAl Layered Double Hydroxides as Catalysts with Enhanced Photodegradation and Antibacterial Activities

Morena Nocchetti [1,*], Monica Pica [1], Berardo Ridolfi [1], Anna Donnadio [1], Elisa Boccalon [2], Giulia Zampini [2], Donatella Pietrella [1] and Mario Casciola [2]

[1] Department of Pharmaceutical Sciences, University of Perugia, Via del Liceo, 1, 06123 Perugia, Italy; monica.pica@unipg.it (M.P.); bero82@libero.it (B.R.); anna.donnadio@unipg.it (A.D.); donatella.pietrella@unipg.it (D.P.)

[2] Department of Chemistry, Biology and Biotechnologies, University of Perugia, Via Elce di Sotto, 8, 06123 Perugia, Italy; elisa.boccalon@studenti.unipg.it (E.B.); giulia.zampini87@gmail.com (G.Z.); mario.casciola@unipg.it (M.C.)

* Correspondence: morena.nocchetti@unipg.it; Tel.: +39-075-585-5562

Received: 18 July 2019; Accepted: 29 September 2019; Published: 3 October 2019

Abstract: Surface-modified ZnAl layered double hydroxides (LDHs) were prepared by reaction of $AgNO_3$, with both ZnAlCl (LDH1) and $ZnAlCO_3$ exchanged on the surface with chloride anions (LDH3). In this way, AgCl nanoparticles with crystalline domains ranging from 40 to 100 nm were grown on the LDH surface. An additional sample was prepared by partial reduction of silver to obtain Ag@AgCl-LDH (LDH2). The composites were tested as catalysts in Rhodamine B (RhB) degradation, wherein LDH2 showed complete cleavage of RhB after 45 min of irradiation versus 70 min needed in the presence of AgCl. This time decreased to 35 min for LDH1 and 15 min for LDH3, underlining the role of the AgCl dimensions and anion in the interlayer region. Studies on the reactive species involved in the degradation process revealed that, for all catalysts, $O_2{\cdot}^-$ was the main active species, while, to some extent, holes contribute to the activity of the LDH3. Finally, the composites showed high bactericidal activity, under irradiation, against *Escherichia coli*, comparable with that of Gentamicin, the positive control. A synergic effect of silver released from the composites and the production of reactive oxygen species was considered.

Keywords: layered double hydroxide; silver chloride; photodegradation; antibacterial; Rhodamine B

1. Introduction

Environmental pollution, with particular attention to water contamination, is a global problem that has led research towards the development of eco-sustainable technologies for environmental remediation. Beside conventional methods, such as adsorption, ultrafiltration, and coagulation, semiconductor-based photocatalysts have received great interest for their stability and efficiency in the oxidation of organic pollutants, including dyes, pesticides and pharmaceuticals [1–3].

Semiconductors, such as TiO_2 and ZnO, show high photocatalytic activity under UV light ($\lambda < 400$ nm), with very limited use of sunlight (about 4%). To overcome this limitation and prepare systems with efficient Vis light harvesting, several strategies have been developed, including non-metal or metal doping of semiconductors and coupling of semiconductors with other materials [4–15].

As well as photo mineralization of organic contaminants, semiconductors possess antibacterial activity due to the production of reactive oxygen species (ROS), such as hydroxyl (OH·), superoxide ($O_2{\cdot}^-$) radicals and hydrogen peroxide (H_2O_2), which are generated upon light absorption [16,17].

Among semiconductor-based photocatalysts, silver halides exhibit excellent photocatalytic performance in the degradation of various organic substances. Moreover, it has been reported that their efficiency can be enhanced when combined with other inorganic materials, acting as either a support or as an active species in the generation of holes and electrons [18–20].

Among inorganic materials, layered double hydroxides (LDHs) represent an intriguing system to support silver halides due to the ease of recovery and preparation. LDHs have a general formula $[M(II)_{1-x}M(III)_x(OH)_2](A^{n-})_{x/n}\cdot H_2O$, where M(II) (M = Mg, Zn, Cu, Ni, Co, etc.) and M(III) (M = Al, Ga, Cr, Mn, In, Fe, etc) are divalent and trivalent metals; x is the molar fraction of the trivalent metal (mol M(III)/(mol M(III) + mol(M(II)), which ranges between 0.2 and 0.4 and determines the charge density of the lamellae, while A^{n-} is the counter anion located in the interlayer gallery [21]. In this context, the preparation of composites constituted by layered double hydroxides and silver/silver halides (Ag/AgX, X = Br, Cl, I) has been explored by Fan et al. [22]. In their study, Co–Ni LDH intercalated with bromide was treated with silver nitrate to precipitate silver bromide and then partially reduced to form the system Ag/AgBr. The resulting composite Ag/AgBr/Co–Ni–NO_3 LDH showed enhanced visible-light photocatalytic activity for photodegradation of methyl orange, Rhodamine B (RhB), and phenol.

Ag/AgCl/Zn–Cr LDHs were prepared by Sun et al. [23] and used as photocatalysts in RhB degradation. The composite showed enhanced visible-light photocatalytic abilities for degradation of organic pollutants in comparison with Ag/AgCl and Zn–Cr LDH.

At the same time our group [24] prepared, with a similar synthetic procedure, composites of Ag/AgCl/ZnAl with good antimicrobial properties against both gram positive and gram negative bacteria and fungi; however, to the best of our knowledge, no photocatalytic activity has been investigated with these composites.

In the present investigation, we report the use of both the chloride and carbonate intercalated ZnAl LDH as support for AgCl nanoparticles (NPs) and their performance as catalysts in RhB degradation. Zn(II) was chosen as the bivalent metal because of the ease of preparation of ZnAl LDH and for its high stability in solution. The effect of the dimension of AgCl NPs, the intercalated anion and the pre-reduction of silver to form Ag@AgCl heterojunction on the photocatalytic process was investigated. The catalysts showed superior performance in comparison with pure AgCl and the degradation of RhB was faster with composites having the smallest AgCl particles and carbonate as the counter anion. Moreover, studies on the recyclability and reactive species involved in the degradation process of RhB were performed. Finally, the anti-bacterial activity of the composites against *Escherichia coli* was also investigated under irradiation and dark conditions, which showed that the light enhanced the ability of the composites to kill bacteria.

2. Results and Discussion

2.1. Characterization of Catalysts

ZnAl LDH containing either carbonate or chloride anions was prepared in a single step by a modified urea method [25]. The XRD spectra of the prepared ZnAlCl and $ZnAlCO_3$ showed the typical patterns (Figure S1). LDHs containing different anions, analyzed by field emission scanning electron microscopy (FE-SEM), exhibit different morphologies: $ZnAlCO_3$ is constituted of hexagonal microcrystals assembled to form a sand-rose morphology with a main dimension of about 2 μm, while ZnAlCl consists of flat hexagonal microcrystals of diameter 2–5 μm and thickness of 200–300 nm. The distinct LDH morphologies are shown in Figure 1.

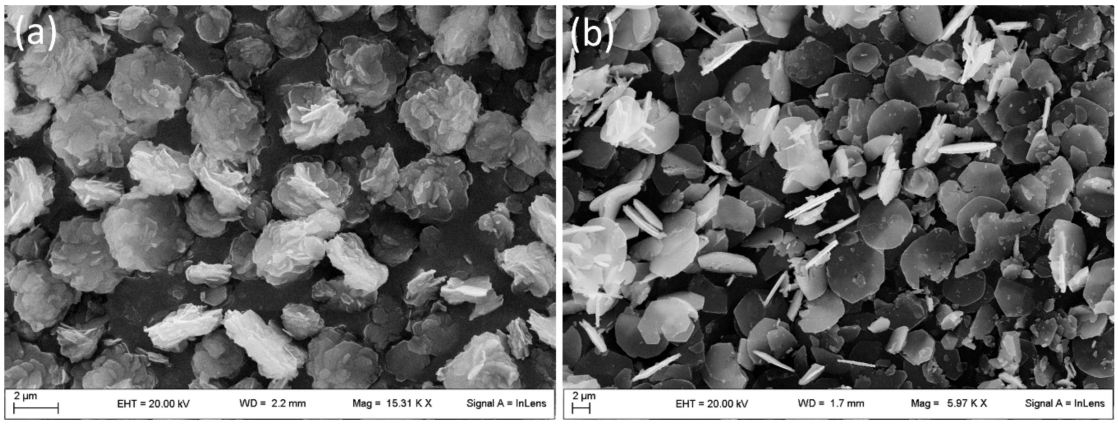

Figure 1. FE-SEM images of $ZnAlCO_3$ (**a**) and ZnAlCl (**b**).

The synthetized LDHs were used as supports of AgCl nanoparticles using a method developed in a previous work [24], from which the basic principles will be recalled here. The method consisted of the addition of a silver nitrate solution to an aqueous dispersion of ZnAlCl. The presence of chloride anions provoked AgCl precipitation on the LDH surface, while the charge balance of LDH was assured by the nitrate anions. A sample named LDH1 was prepared starting from ZnAlCl; the addition of $AgNO_3$ to a ZnAlCl dispersion containing $NaBH_4$ (as reducing agent) gave a sample called LDH2. A sample called LDH3 was prepared starting from $ZnAlCO_3$, which was quickly washed with HCl 10^{-3} M in order to exchange the carbonate anions present on the lamella surface with chloride anions while the interlayer region remained unchanged (see experimental). In this work, no significant variations on the metal content were found, proving that the HCl treatment did not leach the LDH structure. The diffraction patterns of the prepared samples are reported in Figure 2 and show, besides the typical reflections of the LDH phase, additional reflections ascribable to AgCl. In particular, the peaks labeled with the dashed lines were assigned to the crystallographic planes (*111*), (*200*), (*220*), (*311*) and (*222*) of the cubic phase of AgCl by comparison with a reference spectrum (PDF number: 85-1355). The interlayer distance of LDH1 and LDH3 was unchanged with respect to the starting material, suggesting that the exchange of the interlayer carbonate or chloride anions with nitrate was absent or very low; in the latter case, the formation of solid solutions in which the nitrate anions are solubilized in the chloride or carbonate phase could be supposed. Differently, in the sample LDH2, the reflection at 8.9 Å, typical of the nitrate phase of LDH, indicated that a large amount of interlayer chloride anions were substituted by nitrate anions (Figure 2b). In this case, the presence of sodium borohydride in the ZnAlCl dispersion can favor the ion exchange between BH_4^- and Cl^- [26]. When the $AgNO_3$ is added, a part of the silver cations is reduced by the intercalated BH_4^- and the positive charges of the lamellae are neutralized by nitrate anions of the silver salt. The formation of metallic silver was confirmed by the presence of the crystallographic planes (*111*) and (*200*) of its cubic phase in the XRD pattern.

Table 1 reports the amount of silver in the samples, expressed as weight percentage, and the diameter of the AgCl NPs calculated by applying the Debye-Scherrer equation to the (*111*) and (*200*) reflections of the silver chloride cubic phase. The synthetic method used to obtain the composites seemed to affect the dimensions of the AgCl NPs that ranged from 40 to 100 nm. The smallest AgCl NPs were obtained starting from the LDH containing only the chloride anion on the surface.

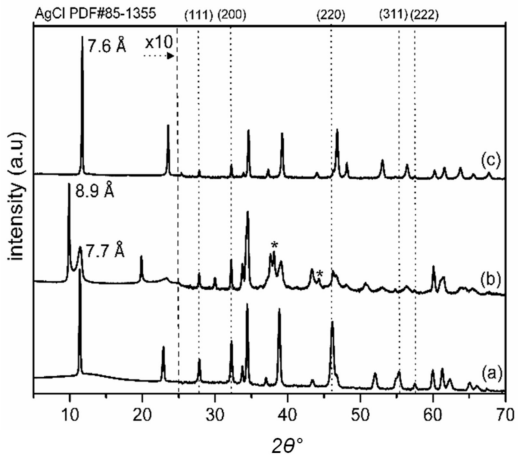

Figure 2. XRD of LDH1 (**a**), LDH2 (**b**) and LDH3 (**c**). The spectral regions, from 25 to 70 2θ°, have been magnified ten times to highlight the AgCl reflections labeled with dashed lines (PDF number: 85-1355). * reflections (*111*) e (*200*) of the cubic phase of metallic silver.

Table 1. Weight percentage of silver and diameter of AgCl of the indicated samples. FWHM: Full width at half maximum.

Sample	Ag (*w*/*w* %)	2θ (°)	FWHM (°)	AgCl Diameter (nm)	
				Calculated [1]	Measured [2] ± SD
LDH1	12.1	27.812 32.224	0.138 0.131	95.2 104.4	94.8 ± 28
LDH2	6.3	27.793 32.202	0.162 0.161	79.2 75.2	65.5 ± 16
LDH3	4.9	27.753 32.160	0.261 0.224	39.2 48.1	64.0 ± 18

[1] By the Debye-Scherrer equation for the Bragg reflections (*111*) and (*200*) of the AgCl cubic phase; [2] Measured by FE-SEM considering 150 nanoparticles.

Figure 3 shows the FE-SEM images of the composites. The composites are characterized by the presence of nanoparticles ascribable to AgCl on the surface of the LDH crystals, which in turn retain the original morphology: flat hexagonal and sand-rose crystals for the chloride and carbonate forms of LDH, respectively. AgCl size distribution, obtained by measuring 150 particles, is also reported in Figure 3, while the mean diameters are indicated in Table 1. The mean diameters of LDH1 and LDH2 were in good agreement with the values obtained by XRD; conversely, LDH3 showed larger particles than the calculated value of the crystal domains, suggesting a polycrystalline character of the particles.

The optical properties of the composites were studied by collecting UV–Vis reflectance spectra and comparing them with that of pure AgCl. As shown in Figure 4, the samples displayed the characteristic absorption of the AgCl below 400 nm, in addition to the absorption band of LDH under 300 nm. In the LDH1 and LDH3 spectra, only the AgCl absorption was detectable, indicating that no Ag NPs were formed. The broad band in the Vis region of the LDH2 spectrum was ascribed to the surface plasmon resonance (SPR) of the silver nanoparticles [27], in agreement with the XRD. The observed SPR covered a wide range of wavelengths due to the contribution of Ag NPs with a broad size distribution and Ag NP aggregates. Moreover, it was found to be centered at 440 nm, indicating the presence of Ag NPs with a diameter of about 30 nm [28] according to the crystalline domain calculated by the Debye-Scherrer equation.

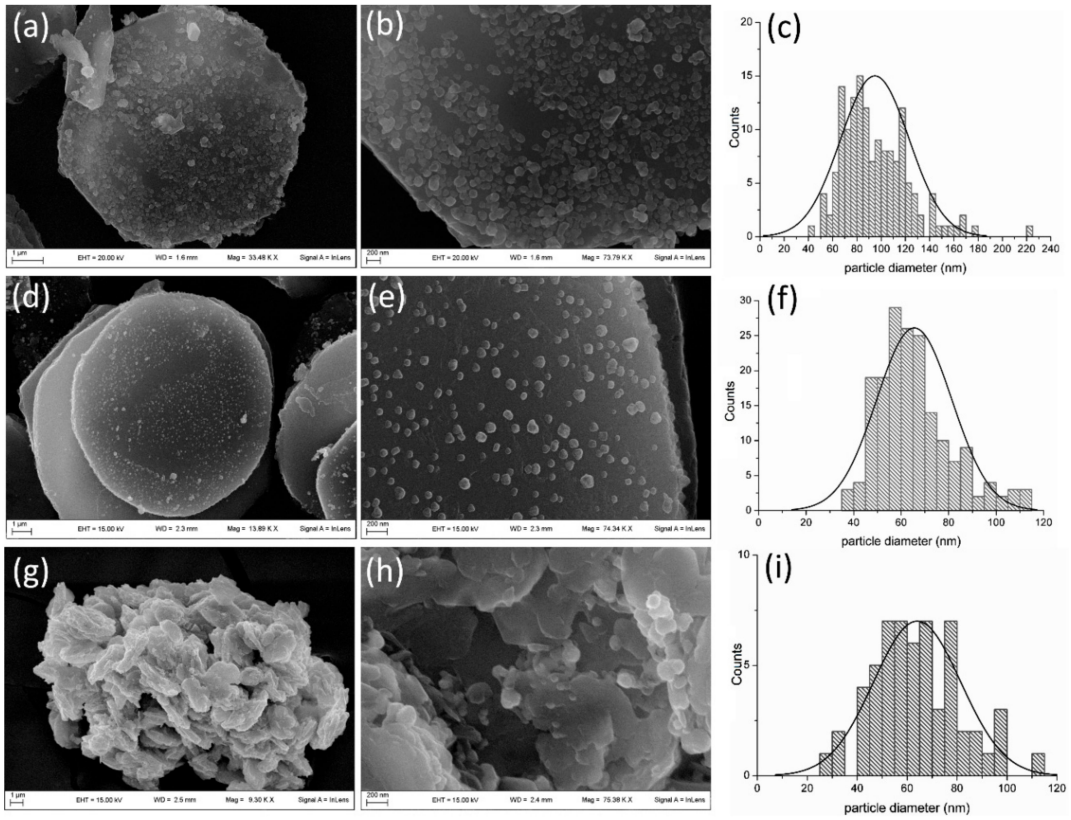

Figure 3. FE-SEM images and size distribution and population of AgCl on layered double hydroxides (LDHs) for: LDH1 (**a**–**c**); LDH2 (**d**–**f**); and LDH3 (**g**–**i**).

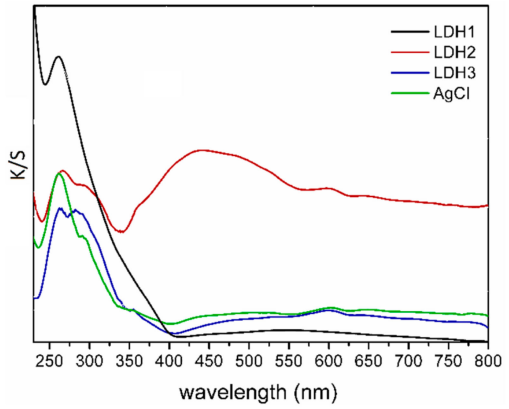

Figure 4. UV–Vis absorption spectra in Kubelka-Munk units of LDH1 (black line), LDH2 (red line), LDH3 (blue line) and AgCl (green line).

2.2. Photodegradation Experiments

The catalytic performance of the composites was investigated using photodegradation of Rhodamine B (RhB), a model dye, in aqueous solution under irradiation with a halogen lamp emitting radiation with $\lambda > 350$ nm. Table 2 reports the amount of catalyst per mL of RhB solution used in different experiments and the estimated half-life ($t_{1/2}$) of RhB.

Table 2. Amount of catalyst and silver per mL of RhB 10^{-5} M and estimated half-life ($t_{1/2}$) of RhB.

Sample	Ag (*w*/*w* %)	mg Sample/mL RhB	mg Ag/mL RhB	RhB $t_{1/2}$ (min)
AgCl	75.3	0.2	0.15	22
LDH1	12.1	1.24	0.15	12
LDH1	12.1	2.48	0.30	<5
LDH2	6.3	2.38	0.15	9
LDH3	4.9	3.06	0.15	<5

To prove the synergic contribution of LDH and silver chloride, control experiments were performed as well. Degradation did not occur in the experiments without the photocatalyst. By using bare ZnAlCl and $ZnAlCO_3$, only modest catalytic activity was observed, even when physically mixed with AgCl (see Table S1 and Figure S2).

Pure AgCl particles did show some activity in the photodegradation of RhB. The tested silver chloride was precipitated in the same conditions used to prepare the AgCl/LDH composite and the solid obtained was characterized by crystals of dimension 1–2 μm (Figure S3). The temporal evolution of the spectral changes of RhB in the presence of pure AgCl is reported in Figure 5A. The absorption spectrum of pure RhB shows a band centered at 554 nm, which decreases after contact with the catalyst in the dark due to adsorption of the dye on the solid surface (spectra at 0 min in Figure 5A). During irradiation, the absorbance of the major absorption band gradually decreases and the position of its maximum moves toward the blue region; the maximum shifts from 554 nm (*N*,*N*,*N*′,*N*′-tetraethylated Rhodamine molecule, RhB) to 498 nm (Rhodamine) [29–32] and the RhB degradation is completed after 80 min irradiation. The blue shift suggests that the degradation of RhB occurs in a stepwise manner in which the ethyl groups are gradually removed to form the de-ethylated species of RhB, which are then cleaved completely.

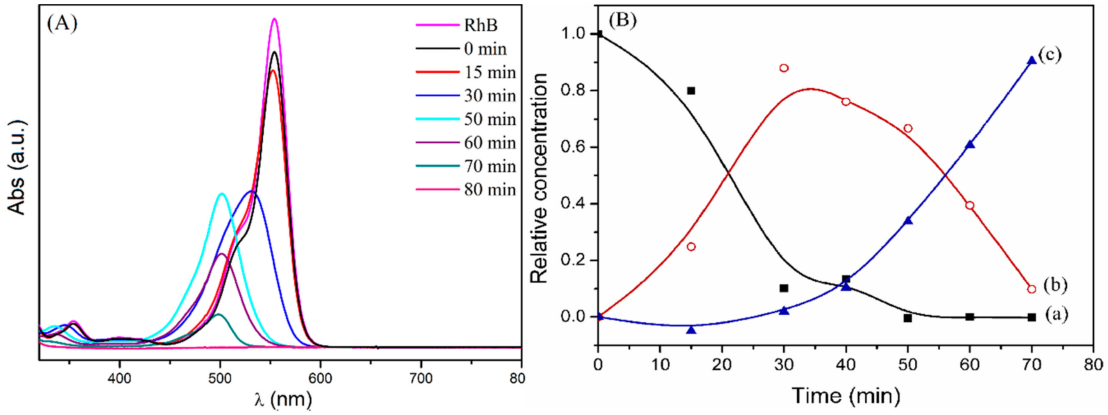

Figure 5. Photodegradation of 10^{-5} M Rhodamine B (RhB) solution by AgCl. (**A**) Temporal evolution of UV–Vis spectra; (**B**) relative concentration of RhB (a), de-ethylated species (b), and cleaved species (c).

In order to get information about the contribution of de-ethylation and cleavage processes during RhB photodegradation, the relative concentration of the de-ethylated species and RhB (calculated as reported in the experimental section) was plotted as a function of irradiation time, as depicted in Figure 5B. As shown in the figure, the concentration of RhB decreases over time, approaching zero after 50 min of irradiation, while the concentration of the de-ethylated species increases up to the maximum value after about 30 min. Then, cleavage of the chromophore group occurs, consuming the de-ethylated species and causing its concentration to decrease and approach zero at 70 min. On the basis of these findings, it can be stated that the degradation process starts mainly with RhB de-ethylation, which is followed by cleavage of the de-ethylated species.

This RhB photodegradation process has been observed in earlier studies [33–36] and seems to depend on the adsorption modes of RhB on the surface of the catalyst. Generally, AgCl particles are negatively charged due to an excess of chloride anions on the surface; accordingly, RhB molecules are adsorbed on the AgCl surface through positively charged diethylamino groups. The reactive oxygen species, produced near the adsorbed RhB, preferentially attack the nearer organic groups, which are the amino groups in this case, thereby leading to de-ethylation.

We then performed kinetic experiments with the composites LDH1, LDH2 and LDH3 in the same conditions used for AgCl (mg Ag/mL RhB = 0.15). The temporal evolution of the RhB absorption band under irradiation (Figure 6A–C) showed that the performance of LDH1, LDH2 and LDH3 was better than that of the pure AgCl, bleaching the RhB solution in 35, 45 and 15 min, respectively.

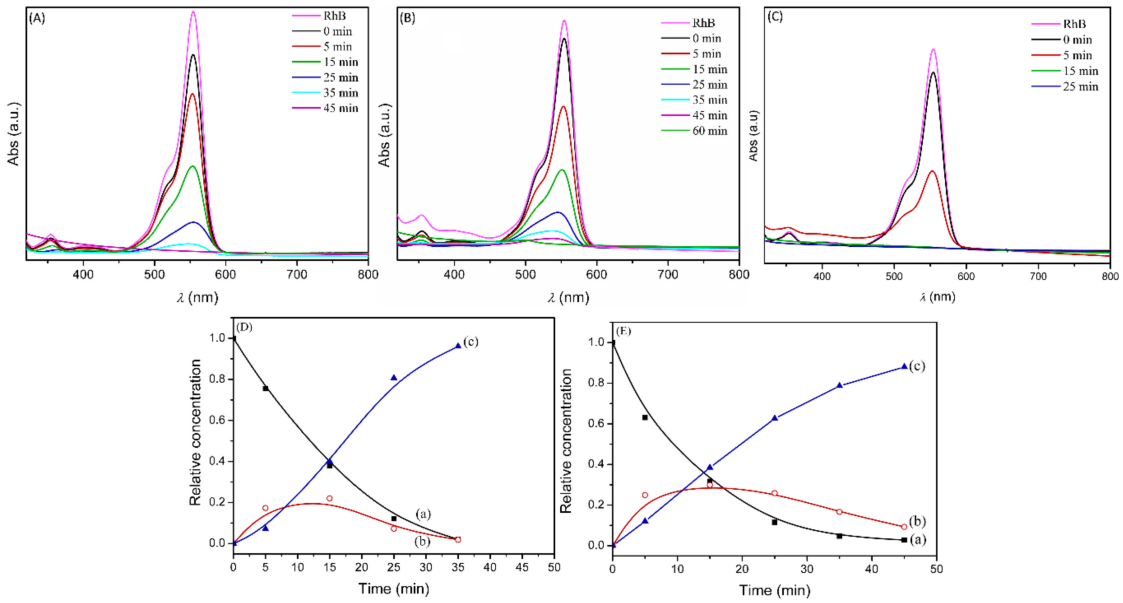

Figure 6. Photodegradation of 10^{-5} M RhB solution by LDH1, LDH2 and LDH3 catalysts (mg Ag/mL RhB = 0.15). Temporal evolution of UV–Vis spectra of LDH1 (**A**), LDH2 (**B**) and LDH3 (**C**); relative concentration of RhB (a), de-ethylated species (b), and cleaved species (c) in the presence of LDH1 (**D**), LDH2 (**E**).

Figure 6A shows that the wavelength of the absorption maximum (λ_{max}) is always centered at 554 nm, indicating that, in the discoloration mechanism, the cleavage process is predominant in the presence of LDH1. Conversely, in the kinetic experiment performed with LDH2, a distinct blue-shift of the λ_{max} to 539 nm occurred after 35 min of irradiation (Figure 6B). In this case, the contribution of the de-ethylation process in the whole degradation procedure seems more consistent than for the previous catalyst. In order to get more quantitative information about the contribution of the de-ethylation and cleavage processes, the relative concentrations of the RhB, de-ethylated and cleaved species (calculated as reported in the experimental section) were plotted as a function of irradiation time in Figure 6D–E for the experiments with LDH1 and LDH2. It can be observed that RhB degradation shows about the same time dependence with both catalysts and that de-ethylation and cleavage occur concomitantly, resulting in more efficient photodegradation processes in comparison with the process catalyzed by pure AgCl. Specifically, de-ethylation prevails over cleavage only during the first few minutes, while the concentration of cleaved species becomes significantly larger than that of de-ethylated species already after about 15 min. Moreover, cleavage is faster with LDH1 so that the concentration of de-ethylated species is always larger with LDH2.

The lack of enough experimental data for the composite LDH3 did not allow us to obtain a concentration trend for the species formed during photodegradation; however, it is possible to compare the data obtained after five minutes since the irradiation started with the corresponding data obtained

with LDH1 and LDH2. The percentage of de-ethylated species in LDH3 (22.5%) was close to that of LDH1 (18%) and LDH2 (25%) catalysts, while the contribution of cleavage to the degradation process was very high (36%) in comparison to the other catalysts (7% for LDH1 and 12% for LDH2), lowering the RhB concentration to 42% of its initial value.

Although the present data did not allow us to establish whether de-ethylation and cleavage with LDH-based catalysts were consecutive or parallel reactions, it is clear that, in comparison with pure AgCl, the presence of ZnAl LDHs made cleavage much more competitive with respect to de-ethylation in the photodegradation process of RhB. Moreover, the presence of ZnAl LDHs appears to speed up the degradation kinetics of RhB, as shown by the RhB half-life ($t_{1/2}$, Table 2), obtained from interpolation of the relative concentration data of RhB. The RhB $t_{1/2}$ was halved in the presence of LDH1 and LDH2 compared with pure AgCl (12 and 9 min versus 22 min, respectively) and was lower than 5 min when LDH3 was used.

The LDH1 and LDH3 catalysts were recovered after the photocatalysis experiments and were analyzed with XRD (Figure 7), revealing a small reflection assignable to metallic silver. This demonstrated that a part of the silver ions underwent a reduction during the irradiation, forming the Ag@AgCl heterojunction.

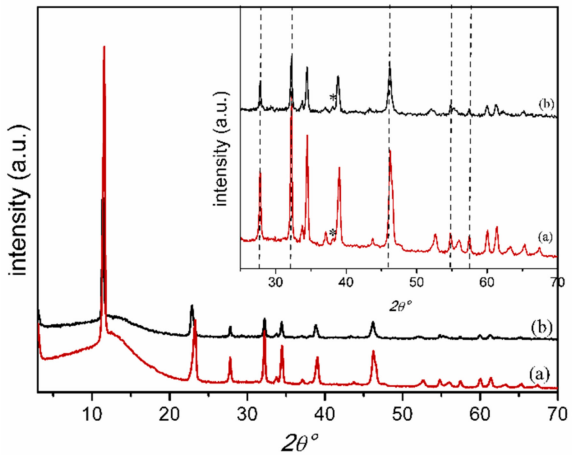

Figure 7. XRD of LDH3 (**a**) and LDH1 (**b**) after the photocatalytic experiments. The spectral regions from 25 to 70 2θ° have been magnified ten times. AgCl (dashed lines), Ag (*).

The superior performance of the AgCl/LDH composites compared to pure AgCl may be attributed to the peculiar characteristics of the composites:

(i) RhB can be adsorbed on the composites through either positive amino groups or carboxylic groups interacting with the negative surface of AgCl or the positive surface of LDH, respectively. The orientation of RhB with the carboxylic groups on the surface of the catalyst favors the attack on the chromophore structure (cleavage) by the reactive species formed on the surface of the catalyst [33]. Conversely, as described above, the adsorption of RhB with the amino groups favors the de-ethylation process. These two different adsorption modes may explain the simultaneous occurrence of the two degradation pathways of the dye.

(ii) The dimensions of AgCl particles grown on the LDH surface are in the nanometric scale, ranging from 40 to 100 nm, more than an order of magnitude smaller than pure AgCl (about 1 μm). Generally, the smaller the particle, the higher the photocatalytic activity due to the increase in the number of active sites [37].

A comparison among the photoactivity of AgCl/LDH composites is useful to select the best catalyst and to get insight into the main factors contributing to the design of an efficient catalyst. LDH3's superior activity may be explained considering the dimensions of AgCl grown on the LDH surface. The diameter of crystalline domains of AgCl particles in LDH3 is 2.3 times smaller than AgCl particles in LDH1 so that, for an equal amount of AgCl, the total surface of AgCl particles in LDH3 is

about 2.3 times larger; this is reflected in the higher number of catalytic sites in LDH3. For proof of the effect of number catalytic sites on photocatalytic performance, a catalytic test with increased LDH1 content was performed (mg Ag/mL RhB = 0.30). The performance of LDH1 increased considerably, bleaching the RhB solution in 15 min, similar to the performance observed for LDH3 (see UV–Vis spectra in Figure S4).

It was interesting to observe that, when the LDH1 concentration was doubled (mg Ag/mL RhB = 0.30), the percentage of RhB after 5 min of irradiation (41.9%, Table 3) was about the same as that found for LDH3 (41.6%) with mg Ag/mL RhB = 0.15. However, the percentage of de-ethylated species (38.8%) in LDH1 was larger than that of LDH3 (22.5%), so that the contribution of cleavage in LDH1 was smaller (19.3%) in comparison with LDH3 (35.9%).

Table 3. RhB, de-ethylation, cleavage percentage and ratio between the percentage of cleaved and de-ethylated species after 5 min since start of irradiation for LDH1 (mg Ag/mL RhB = 0.30) and LDH3 (mg Ag/mL RhB = 0.15).

Run	% RhB		% De-Ethylated		% Cleavage		% Cleav/% De-eth	
	LDH1	LDH3	LDH1	LDH3	LDH1	LDH3	LDH1	LDH3
I	41.9	41.6	38.8	22.5	19.3	35.9	0.50	1.6
II	43.5	24.4	31.9	17.8	24.6	57.8	0.77	3.2
III	17.2	8.2	54.3	25.0	28.5	66.8	0.52	2.7

2.3. Recyclability of the Catalysts

The stability and possibility of recovering and reusing a catalyst is a crucial factor in practical applications. The AgCl/LDH composites are easily recuperated by centrifugation thanks to the micrometric dimension of the LDHs that efficiently support the nanometric AgCl. Tests of recyclability were carried out with LDH1 (mg Ag/mL RhB = 0.30) and LDH3 (mg Ag/mL RhB = 0.15) catalysts and the relative concentration of RhB in solution was plotted as function of irradiation time (Figure 8). The catalysts showed very good stability and even improved efficiency until the third run of catalysis. Moreover, the percentage of de-ethylated and cleaved species after five min irradiation (Table 3) confirmed that cleavage was favored by LDH3, with the ratio between the percentage of cleaved and de-ethylated species being in the range 0.50–0.77 for LDH1 and 1.6–2.7 for LDH3.

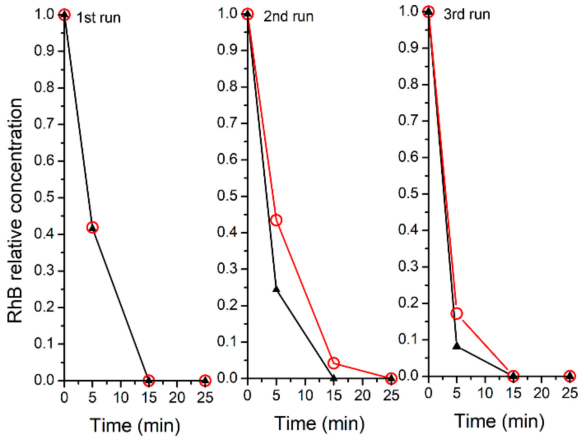

Figure 8. Cycling runs in the photodegradation of RhB in the presence of LDH1 (mg Ag/mL RhB = 0.30; red circle) and LDH3 (mg Ag/mL RhB = 0.15; black triangle).

2.4. Mechanism of Photocatalytic Degradation

The identification of the reactive species involved in the degradation process of RhB allowed us to get insight into the reaction mechanism in the presence of our catalysts. To this end, experiments of

photodegradation in the presence of radical scavengers, including benzoquinone (BQ) for the superoxide radical anion ($O_2{\cdot}^-$), isopropanol (IPA) for the hydroxyl radical (OH·) and ethylenediaminetetraacetic acid disodium salt (Na_2-EDTA) for the positively charged vacancy or hole (h^+), were carried out. Figure 9 shows that the photoactivity of all of the catalysts was dramatically suppressed in the presence of BQ, indicating the superoxide anion was the main active species in the photochemical process.

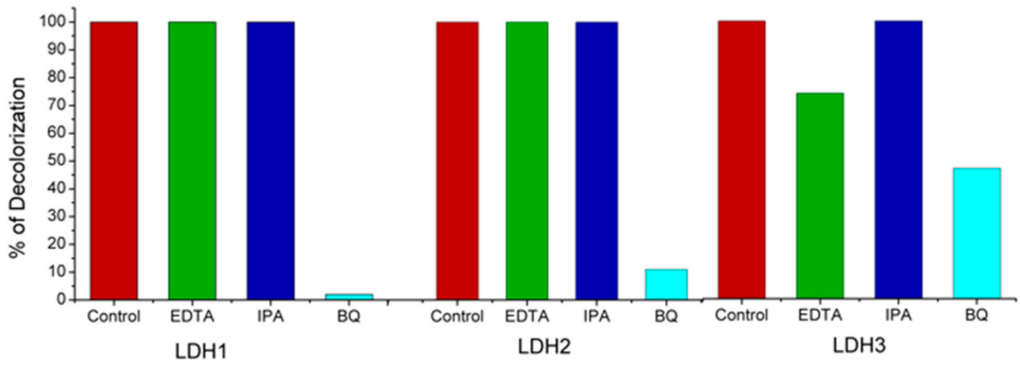

Figure 9. Photodegradation tests of RhB with different quenchers in the presence of the indicated catalysts.

On the other hand, photodegradation in the presence of LDH3 was hindered by EDTA, although to a lesser degree than BQ, indicating that h^+ may also be involved in the process.

According to the literature, the superoxide anion can mainly be formed through a photosensitized mechanism [38–40], wherein the first step is the absorption of light by the dye to induce an intramolecular π–π transition. Once RhB is excited, it transfers its electron to the inorganic matrix, forming an RhB radical cation [41]. More specifically, the electron is expected to be accommodated in the conduction band (CB) of AgCl, for which the redox potential vs. normal hydrogen electrode (NHE) (−0.09 V [42]) is higher than that of ZnAl LDH (−2.0 V [43]). Subsequently, it can be transferred to an oxygen molecule adsorbed on AgCl to form the superoxide anion $O_2{\cdot}^-$, due to the higher potential of the $O_2/O_2{\cdot}^-$ redox couple (−0.046 V vs. NHE [42]). The superoxide anion can also diffuse along the LDH surface through an interchange reaction with the LDH anions and, finally, react with the radical cation of the dye (adsorbed either on AgCl or LDH), provoking degradation of the dye.

As mentioned in Section 2.2, the position of the dye that is preferentially attacked by $O_2{\cdot}^-$ is the group of the dye interacting with the surface of the catalyst; i.e., the carboxylic group or the amino group for dye adsorption on LDH or AgCl, respectively.

Moreover, due the presence of metallic silver in all the LDH samples, an SPR-mediated charge transfer process should be considered alongside the dye photosensitized mechanism [44]. Silver plasmonic nanoparticles, in direct contact with the AgCl surface, act as a dye sensitizer, absorbing resonant photons that generate electron-hole pairs in Ag nanocrystals. The surface of AgCl particles is negatively charged due the presence of terminal Cl^- ions, thereby polarizing the electronic distribution of Ag NPs and moving the plasmon-excited electrons on the surface of the Ag NPs far from the Ag/AgCl interface and the holes to the surface of the AgCl NPs [18,45,46]. The photogenerated electrons are trapped by O_2 to form $O_2{\cdot}^-$, leading to dye degradation.

Finally, considering that AgCl has an indirect band gap of 3.25 eV [47], electron–hole pairs can be generated by the absorption of photons with λ in the range 350–382 nm. This process, which is clearly not relevant for RhB degradation in the presence LDH1, could become significant for LDH3 because it has been reported that the carbonate anion reduces electron–hole recombination [48].

2.5. Antibacterial Activity of Catalysts

In a previous work [24], we found that AgCl/LDH composites exhibited very good antimicrobial activity against bacteria and fungi. Here, it was of interest to test the antibacterial activity of the

best catalysts, LDH1 and LDH3, against *Escherichia coli*, a typical water contaminant. Table 4 shows the minimum inhibitory concentration required to inhibit the growth of 90% of bacteria (MIC90); gentamicin and LDH were used as negative and positive controls, respectively.

Table 4. Antibacterial activity (MIC90) of LDH1 and LDH3 catalysts.

Sample	MIC90 ($\mu g \cdot ml^{-1}$)
LDH1	9.45
LDH3	3.83
LDH	>10000
Gentamicin	<0.12

The samples showed good antibacterial activity, even if they were lower than that of the positive control, gentamicin. The best antibacterial activity was expressed by LDH3, in agreement with the lower dimensions of the AgCl NPs, which correspond to greater surface area and thereby promote better contact with the bacteria [49].

Kinetic experiments of the antibacterial activity of LDH1 and LDH3 in the dark and under irradiation ($\lambda > 350$ nm) were performed at the concentrations of MIC90 (Table 4). The time–kill curves, reported in Figure 10, showed that the number of live bacteria was already considerably reduced after 60 min in the presence of LDH1 and LDH3 under irradiation. It is noteworthy that the curves were superimposable with those of gentamicin in the dark, suggesting that the antibacterial activity of the catalysts under irradiation were comparable to those of the positive control. On the other hand, no reduction in bacteria was observed until 180 min for the catalysts in the dark or for the bacteria cultures both irradiated and in the dark in the absence of the catalysts. The high antibacterial activity of the catalysts under irradiation for a very short time can be explained by the formation of Ag clusters on AgCl (Figure 7) and the production of reactive oxygen species (ROS), such as $O_2 \cdot^-$, also observed in the photodegradation of RhB. The antibacterial activity of the composites is significantly enhanced due to a synergic effect of ROS and silver ions [50,51].

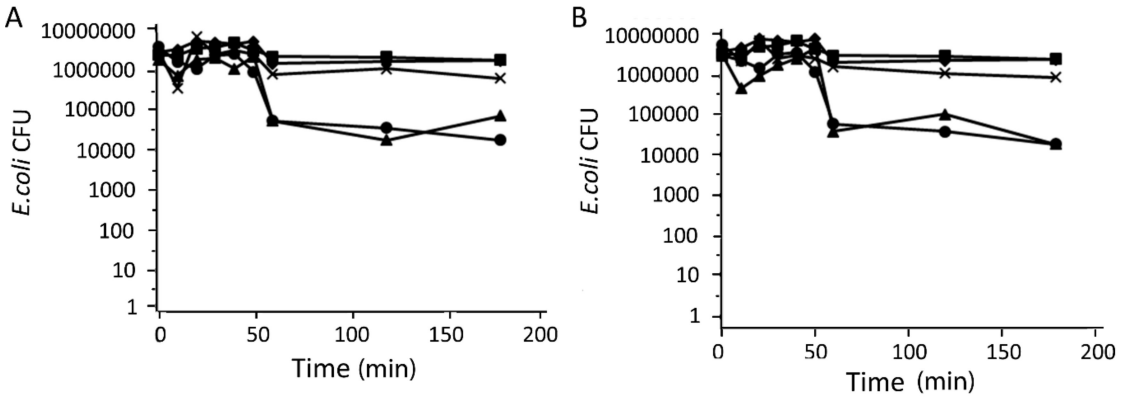

Figure 10. Time-kill curves of LDH1 (**A**) and LDH3 (**B**) composites against *E. coli*. Cells were untreated in the dark (−♦−) and under irradiation (−■−); treated with the MIC of LDH1 or LDH3 in the dark (− × −) and under irradiation (−▲−); treated with gentamicin in the dark (−●−) for different time periods.

3. Materials and Methods

3.1. Chemicals

Rhodamine B chloride was supplied by Aldrich (Milano, Italy). All other chemicals were C. Erba RP-ACS products (Milano, Italy). Reagents and solvents were of reagent grade and were used without further purification. Muller Hinton Broth (MHB) and Muller Hinton Agar (MHA) were provided by Biolife (Milan, Italy).

3.2. Catalysts Synthesis

Layered double hydroxides with formula $[Zn_{0.67}Al_{0.33}(OH)_2](Cl)_{0.33}{\cdot}0.6H_2O$ (ZnAlCl) and $[Zn_{0.67}Al_{0.33}(OH)_2](CO_3)_{0.}165{\cdot}0.6H_2O$ ($ZnAlCO_3$) were prepared as reported in Ref. [27,52], respectively. To begin with, 32 mL of 0.05 M $AgNO_3$ aqueous solution was added dropwise to a dispersion of 2 g of ZnAlCl in 160 mL of de-ionized water under stirring. The suspension was kept under stirring for 24 hrs. The solid (hereafter LDH1) was recovered by centrifugation (15,000 rpm for 15 min) and was washed two times with de-ionized water. Finally, LDH1 was dried in a desiccator, over P_4O_{10}. All the operations were conducted in the dark. A sample, named LDH2, was prepared as described above with the exception of the addition of 32 mL of 0.05 M $NaBH_4$ to the ZnAlCl dispersion, before the reaction with silver nitrate. An additional sample, named LDH3, was prepared starting from $ZnAlCO_3$. Firstly, 2 g of $ZnAlCO_3$ was dispersed in de-ionized water, filtered and then quickly washed with 20 mL of 10^{-3} M HCl. The recovered solid was dried over P_4O_{10} and treated with $AgNO_3$, as was the LDH1 sample.

Pure AgCl was precipitated from 0.05 M $AgNO_3$ aqueous solution by adding 0.5 M HCl (Cl/Ag molar ratio = 30). The solid was recovered by centrifugation and washed with 10^{-3} M HCl, dried over P_4O_{10} and used as a reference material.

3.3. Instrumental Procedures

The samples were characterized by inductively coupled plasma-optical emission spectrometers (ICP-OES), X-ray powder diffraction (XRD), a transmission electron microscope (TEM), a scanning electron microscope (SEM) and a UV–Vis spectrophotometer.

XRD patterns were recorded by a Philips X'PERT PRO MPD diffractometer (PANalytical, Royston, UK) operating at 40 kV and 40 mA, with a step size 0.0170 2θ degree, and step scan 20 s, using Cu Kα radiation and an X'Celerator detector. The diameter of the AgCl NPs were calculated applying the Debye-Scherrer equation $D = (0.9 \times \lambda)/(\delta \times \cos\theta)$ (λ = incident ray wavelength: 1.54050 Å; δ = FWHM correct for instrumental broadening considering the width of LaB_6 standard profile; θ = diffraction angle) to the (*111*) and (*200*) reflections of the silver chloride cubic phase.

Metal analyses were performed with a ICP-OES spectrometer (Varian 700-ES series, Santa Clara, CA, USA). Firstly, 20 mg of ZnAl LDH was dissolved in concentrated HNO_3 and de-ionized water until a final volume of 100 mL. The solution, properly diluted, was analyzed by ICP. The sample containing silver was treated with ammonia (1 mL of ammonia for 10 mg of sample) for 12 hrs. The dispersion was diluted with 50 mL of de-ionized water and the solution, separated by filtration, was analyzed by ICP.

The morphology of the samples was investigated with a transmission electron microscope (TEM, Philips 208, Eindhoven, Nederland) and with a scanning electron microscope (FE-SEM, FEG LEO 1525). For the TEM images, a small drop of the aqueous dispersion was deposited on a copper grid precoated with a Formvar film and then evaporated in air at room temperature. FE-SEM micrographs were collected after depositing the dry samples on a stub and sputter coating with chromium for 20 s.

Absorption spectra of the samples were recorded by a Varian (Cary 4000) spectrophotometer (Santa Clara, CA, USA), equipped with a 150 mm integration sphere, for which a barium sulphate tablet was used as a reference. The recorded spectra were analyzed with the Kubelka-Munk equation in order to make the comparison possible.

3.4. Photodegradation Experiments

The catalytic activity of LDH1, LDH2 and LDH3 was tested by following the photodegradation of the dye Rhodamine B (RhB). A weighted amount of catalyst was suspended in a 25 mL aqueous solution of RhB 10^{-5} M. The mixture was equilibrated in darkness for 30 min to ensure the adsorption equilibrium of RhB on the catalyst. After this, the mixture was irradiated with a 105 W Osram halogen lamp with a UV filter providing radiation with λ > 350 nm (UV light emitted by the lamp is less than

2% of the visible light). The lamp was placed 7.5 cm from the dispersion surface and the irradiated area was 16 cm^2. From the dispersion, 3 mL of solution was withdrawn at regular time intervals and centrifuged (15,000 rpm for 15 min) to remove the solid portion. The recovered solution was analyzed by UV–Vis spectrometry. Table 2 reports the amount of catalyst used in the catalytic tests. The results of the photocatalytic experiments are reported as relative concentration of RhB, de-ethylated and cleaved species, calculated as described in one of our recent papers [20]. The cleaved species adsorbed in the UV region, while RhB and its de-ethylated species in the 450–600 nm region. Therefore, only RhB (λ_{max}= 554 nm) and the de-ethylated species (*N*,*N*,*N*′-tri-ethylated Rhodamine λ_{max} = 539 nm; *N*,*N*′-di-ethylated Rhodamine λ_{max} = 522 nm; *N*-ethylated Rhodamine, λ_{max} = 510 nm; and Rhodamine λ_{max} = 498 nm) contribute to the absorbance at time *t* ($A_\lambda(t)$) in the Vis region [29]. $A_\lambda(t)$ can be written as:

$$A_\lambda(t) = d\sum_{i=1}^{5} \varepsilon_{i,\lambda} C_i(t), \quad (1)$$

where: *d* = path length of the light beam; $\varepsilon_{i,\lambda}$ = molar extinction coefficient of the *i* species at the wavelength λ: *i* = 1 for RhB, *i* = 2 for *N*,*N*,*N*′-triethylated Rh, *i* = 3 for *N*,*N*′-diethylated Rh, *i* = 4 for *N*-ethylated Rh and *i* = 5 for Rh. $C_i(t)$ = concentration of the *i* at time *t*.

For each spectrum at time t, the values of the absorbance at λ_{max} of the five species present in the photocatalyzed solution were determined. The five experimental values of absorbance ($A_\lambda(t)$) were expressed as in Equation (1) using the molar extinction coefficients for each wavelength ($\varepsilon_{i,\lambda}$), derived from the Watanabe paper [29]. In this way, a system of five linear equations was obtained for which the solution provided the five unknown concentrations. The solution of the system allows the calculation, as a function of time, of the RhB relative concentration:

$$C_1(t)/C_1(0), \quad (2)$$

where $C_1(0)$ is the concentration of RhB at *t* = 0 min.

The relative total concentration of the de-ethylated species is:

$$\sum_{i=2}^{5} C_i(t)/C_1(0), \quad (3)$$

The relative concentration of the cleaved species is:

$$1 - \sum_{i=1}^{5} C_i(t)/C_1(0), \quad (4)$$

Experiments of dye photodegradation were performed, adding to the dye solution 10^{-5} M quenchers with a concentration of 10^{-3} M. Di-sodium salt of ethylenediaminetetraacetic acid (EDTA), 2-propanol (IPA) and benzoquinone (BQ) were used as scavenger of holes (h^+), hydroxyl radicals (OH·) and superoxide radicals ($O_2{\cdot}^-$), respectively. The dye/quencher solutions were irradiated in the presence of the catalysts, in the same conditions described above, for as long as necessary to decolor the dye solution without quenchers.

3.5. Antimicrobial Performance Test

The antimicrobial activity was determined by the dilution susceptibility testing methods following standard Clinical and Laboratory Standards Institute (CLSI) methods. The samples tested were LDH1 and LDH3; the silver content in the samples was 12.1 and 4.9% *w*/*w*, respectively. Quantitative analyses were performed in triplicate for *Escherichia coli DH5 alpha* (ATCC 67878). Microbial inocula were prepared by subculturing bacteria in Muller Hinton Broth (MHB) at 37 °C for 18 h and then diluted to approximately 10^5–10^6 organisms per ml. Samples of 100 µL were serially diluted in 1:2 ratio in

an appropriate medium MHB and placed in a 96-well tissue culture plate. The initial concentration of compounds used was 10 mg/mL. Test microorganism aliquots of 10 µL were added to each well; microplates were then incubated at 37 °C for 24 h. The results are reported as a minimum inhibitory concentration required to inhibit the growth of 90% of microorganisms and normalized on the basis of the total silver content.

3.6. Time-Kill Curve Experiments

To confirm the microbicidal activity of LDH1 and LDH3 composites, time-kill procedures were performed for *E. coli* in the dark or irradiated with the lamp used in the photocatalytic experiments placed 7 cm away from the plate surface. Cells sub-cultured in MHB at 37 °C for 18 h were centrifuged, washed and resuspended at a concentration of 2×10^7 cells per ml, supplemented with LDH1 or LDH3 and incubated at 37 °C in the dark and under irradiation. The catalyst concentrations used in the test were equivalent to the MIC. At predetermined time points (0, 10, 20, 30, 40, 50, 60, 120, 180 min) of incubation, 100 µL aliquots were removed from the test solution and serial dilutions were performed. Aliquots of 100 µL from each dilution were spread on the surface of Muller Hinton Agar (MHA) plates and incubated at 37 °C for 48 h for the determination of CFU per ml. Gentamicin and ZnAlCl were used as positive and negative control, respectively.

4. Conclusions

In this work, ZnAlCl and $ZnAlCO_3$ were used as support for AgCl NPs and the composites obtained were tested as catalysts in the photodegradation of RhB. The catalysts showed superior performances with respect to pure AgCl, recyclability and even an improved efficiency until the third run of catalysis. The high activity was attributed to the nanometric dimensions of AgCl grown on the LDH surface (40–100 nm), compared to pure AgCl (about 1 µm). Studies on the relative concentration of RhB, de-ethylated and cleaved species formed during the photodegradation process highlighted that, in comparison with pure AgCl, the presence of ZnAl LDHs favors the cleavage process with respect to the de-ethylation. This photodegradation pathway may be attributed to the adsorption of RhB on the LDH surface by the carboxylic group, which exposes the chromophore structure to the reactive species formed on the surface of the catalyst. Experiments on the reactive species involved in the photodegradation process showed that for all of the catalysts, the $O_2^{\bullet -}$ species was the main active species involved in RhB degradation, with a non-negligible contribution of h^+ for the LDH3 composite. A comparison among the catalysts showed that LDH3 was the most efficient catalyst for the photodegradation of RhB, likely because it supports the smallest AgCl NPs and possesses in the interlayer region carbonate anions that may reduce electron-hole recombination. Finally, the formation of ROS during irradiation enhanced the antibacterial activity of LDH1 and LDH3 towards *E. coli*, making it similar to that of gentamicin.

Supplementary Materials: The following are available online at http://www.mdpi.com/2304-6740/7/10/120/s1, Figure S1: XRD of ZnAl–CO3 and ZnAl–Cl, Figure S2: Degradation kinetics of RhB in the presence of ZnAlCl, $ZnAlCO_3$, ZnAlCl/AgCl and $ZnAlCO_3$/AgCl physical mixture, Figure S3: SEM images of pure AgCl, Figure S4: Photodegradation of 10^{-5} M RhB solution by LDH1 catalyst (mg Ag/mL RhB = 0.30). Temporal evolution of UV–Vis spectra during the first run, second run and third run, Figure S5: Photodegradation of 10^{-5} M RhB solution by LDH3 catalyst (mg Ag/mL RhB = 0.15). Temporal evolution of UV–Vis spectra during the first run, second run and third run, Table S1: Amount of catalyst and silver per mL of RhB 10^{-5} M.

Author Contributions: Conceptualization, M.N., M.P. and A.D.; Data curation, M.N. and M.C.; Investigation, M.N., B.R., E.B., G.Z. and D.P.; Writing—original draft, M.N.

Funding: This research was funded by MIUR within the AMIS and DELPHI projects through the program "Dipartimenti di Eccellenza 2018-2022".

Conflicts of Interest: The authors declare no conflict of interest.

References

1. Litter, M.I.; Candal, R.J.; Meichtry, J.M. (Eds.) *Advanced Oxidation Technologies—Sustainable Solutions for Environmental Treatments*, 1st ed.; CRC Press/Balkema: Leiden, The Netherlands, 2014; Volume 9.
2. Amin, M.T.; Alazba, A.A.; Manzoor, U. A Review of Removal of Pollutants from Water/Wastewater Using Different Types of Nanomaterials. *Adv. Mater. Sci. Eng.* **2014**, *2014*, 825910. [CrossRef]
3. Chiu, Y.H.; Chang, T.F.M.; Chen, C.Y.; Sone, M.; Hsu, Y.J. Mechanistic Insights into Photodegradation of Organic Dyes Using Heterostructure Photocatalysts. *Catalysts* **2019**, *9*, 430. [CrossRef]
4. Wu, M.J.; Wu, J.Z.; Zhang, J.; Chen, H.; Zhou, J.Z.; Qian, G.R.; Xu, Z.P.; Du, Z.; Rao, Q.L. A review on fabricating heterostructures from layered double hydroxides for enhanced photocatalytic activities. *Catal. Sci. Technol.* **2018**, *8*, 1207–1228. [CrossRef]
5. Lin, W.-H.; Chiu, Y.-H.; Shao, P.-W.; Hsu, Y.-J. Metal-Particle-Decorated ZnO Nanocrystals: Photocatalysis and Charge Dynamics. *ACS Appl. Mater. Interfaces* **2016**, *8*, 32754–32763. [CrossRef]
6. Chen, Y.-C.; Liu, T.-C.; Hsu, Y.-J. $ZnSe{\cdot}0.5N_2H_4$ Hybrid Nanostructures: A Promising Alternative Photocatalyst for Solar Conversion. *ACS Appl. Mater. Interfaces* **2015**, *7*, 1616–1623. [CrossRef]
7. Pu, Y.-C.; Chou, H.-Y.; Kuo, W.-S.; We, K.-H.; Hsu, Y.J. Interfacial charge carrier dynamics of cuprous oxide-reduced graphene oxide (Cu_2O-rGO) nanoheterostructures and their related visible-light-driven photocatalysis. *Appl. Catal. B Environ.* **2017**, *204*, 21–32. [CrossRef]
8. Pu, Y.-C.; Lin, W.-H.; Hsu, Y.-J. Modulation of charge carrier dynamics of $Na_xH_{2-x}Ti_3O_7$–Au–Cu_2O Z-scheme nanoheterostructures through size effect. *Appl. Catal. B Environ.* **2015**, *163*, 343–351. [CrossRef]
9. Nguyen, A.T.; Lin, W.-H.; Lu, Y.-H.; Chiou, Y.-D.; Hsu, Y.-J. First demonstration of rainbow photocatalysts using ternary$Cd_{1-x}Zn_xSe$ nanorods of varying compositions. *Appl. Catal. A General.* **2014**, *476*, 140–147. [CrossRef]
10. Chen, M.-Y.; Hsu, Y.-J. Type-II nanorod heterostructure formation through one-step cation exchange. *Nanoscale* **2013**, *5*, 363–368. [CrossRef]
11. Lin, Y.-F.; Hsu, Y.-J. Interfacial charge carrier dynamics of type-II semiconductor nanoheterostructures. *Appl. Catal. B Environ.* **2013**, *130*, 93–98. [CrossRef]
12. Guo, J.-L.; Chiou, Y.-D.; Liang, W.-I.; Liu, H.-J.; Chen, Y.-J.; Kuo, W.-C.; Tsai, C.-Y.; Tsai, K.-A.; Kuo, H.-H.; Hsieh, W.-F.; et al. Complex Oxide–Noble Metal Conjugated Nanoparticles. *Adv. Mater.* **2013**, *25*, 2040–2044. [CrossRef] [PubMed]
13. Chen, Y.-C.; Pu, Y.-C.; Hsu, Y.-J. Interfacial Charge Carrier Dynamics of the Three-Component In_2O_3–TiO_2–Pt Heterojunction System. *J. Phys. Chem. C* **2012**, *116*, 2967–2975. [CrossRef]
14. Chen, W.-T.; Hsu, Y.-J. L-Cysteine-Assisted Growth of Core-Satellite ZnS-Au Nanoassemblies with High Photocatalytic Efficiency. *Langmuir* **2010**, *26*, 5918–5925. [CrossRef] [PubMed]
15. Pu, Y.-C.; Chen, Y.-C.; Hsu, Y.-J. Au-decorated $Na_xH_{2-x}Ti_3O_7$ nanobelts exhibiting remarkable photocatalytic properties under visible-light illumination. *Appl. Catal. B Environ.* **2010**, *97*, 389–397. [CrossRef]
16. Keane, D.A.; McGuigan, K.G.; Ibáñez, P.F.; Polo-López, M.I.; Byrne, J.A.; Dunlop, P.S.M.; O'Shea, K.; Dionysiou, D.D.; Pillai, C.S. Solar photocatalysis for water disinfection: Materials and reactor design. *Catal. Sci. Technol.* **2014**, *4*, 1211–1226. [CrossRef]
17. Tobaldi, D.M.; Piccirillo, C.; Pullar, R.C.; Gualtieri, A.F.; Seabra, M.P.; Castro, P.M.L.; Labrincha, J.A. Silver-Modified Nano-titania as an Antibacterial Agent and Photocatalyst. *J. Phys. Chem. C* **2014**, *118*, 4751–4766. [CrossRef]
18. Wang, P.; Huang, B.; Dai, Y.; Whangbo, M.-H. Plasmonic photocatalysts: Harvesting visible light with noble metal nanoparticles. *Phys. Chem. Chem. Phys.* **2012**, *14*, 9813–9825. [CrossRef] [PubMed]
19. Pica, M.; Nocchetti, M.; Ridolfi, B.; Donnadio, A.; Costantino, F.; Gentili, P.L.; Casciola, M. Nanosized zirconium phosphate/AgCl composite materials: A new synergy for efficient photocatalytic degradation of organic dye pollutants. *J. Mater. Chem. A* **2015**, *3*, 5525–5534. [CrossRef]
20. Pica, M.; Calzuola, S.; Donnadio, A.; Gentili, P.L.; Nocchetti, M.; Casciola, M. De-Ethylation and Cleavage of Rhodamine B by a Zirconium Phosphate/Silver Bromide Composite Photocatalyst. *Catalysts* **2019**, *9*, 3. [CrossRef]
21. Rives, V. (Ed.) *Layered Double Hydroxides: Present and Future*; Nova Science Publishers: New York, NY, USA, 2001.

22. Fan, H.; Zhu, J.; Sun, J.; Zhang, S.; Ai, S. Ag/AgBr/Co–Ni–NO_3 Layered Double Hydroxide Nanocomposites with Highly Adsorptive and Photocatalytic Properties. *Chem. Eur. J.* **2013**, *19*, 2523–2530. [CrossRef]
23. Sun, J.; Zhang, Y.; Cheng, J.; Fan, H.; Zhu, J.; Wang, X.; Ai, S. Synthesis of Ag/AgCl/Zn–Cr LDHs composite with enhanced visible-light photocatalytic performance. *J. Mol. Catal. A Chem.* **2014**, *382*, 146–153. [CrossRef]
24. Nocchetti, M.; Donnadio, A.; Ambrogi, V.; Andreani, P.; Bastianini, M.; Pietrella, D.; Latterini, L. Ag/AgCl nanoparticle decorated layered double hydroxides: Synthesis, characterization and antimicrobial properties. *J. Mater. Chem. B* **2013**, *1*, 2383–2393. [CrossRef]
25. Bastianini, M.; Costenaro, D.; Bisio, C.; Marchese, L.; Costantino, U.; Vivani, R.; Nocchetti, M. On the Intercalation of the Iodine–Iodide Couple on Layered Double Hydroxides with Different Particle Sizes. *Inorg. Chem.* **2012**, *51*, 2560–2568. [CrossRef] [PubMed]
26. Madusanka, N.; Sandaruwan, C.; Kottegoda, N.; Karunaratne, V. Synthesis of Ag Nanoparticle/Mg–Al-Layered Double Hydroxide Nanohybrids. *Eur. Int. J. Appl. Sci. Technol.* **2014**, *1*, 1–7.
27. Ambrogi, V.; Donnadio, A.; Pietrella, D.; Latterini, L.; Alunni Proietti, F.; Marmottini, F.; Padeletti, G.; Kaciulis, S.; Giovagnoli, S.; Ricci, M. Chitosan films containing mesoporous SBA-15 supported silver nanoparticles for wound dressing. *J. Mater. Chem. B* **2014**, *2*, 6054–6063. [CrossRef]
28. Mock, J.J.; Barbic, M.; Smith, D.R.; Schultz, D.A.; Schultz, S. Shape effects in plasmon resonance of individual colloidal silver nanoparticles. *J. Chem. Phys.* **2002**, *116*, 6755–6759. [CrossRef]
29. Watanabe, T.; Takizawa, T.; Honda, K. Photocatalysis through excitation of adsorbates. 1. Highly efficient N-deethylation of rhodamine B adsorbed to cadmium sulfide. *J. Phys. Chem.* **1977**, *81*, 1845–1851. [CrossRef]
30. Inoue, T.; Watanabe, T.; Fujishima, A.; Honda, K.; Kohayakawa, K. Suppression of Surface Dissolution of CdS Photoanode by Reducing Agents. *J. Electrochem. Soc.* **1977**, *124*, 719–722. [CrossRef]
31. Wu, T.; Liu, G.; Zhao, J.; Hidaka, H.; Serpone, N. Photoassisted Degradation of Dye Pollutants. V. Self-Photosensitized Oxidative Transformation of Rhodamine B under Visible Light Irradiation in Aqueous TiO_2 Dispersions. *J. Phys. Chem. B* **1998**, *102*, 5845–5851. [CrossRef]
32. Yang, T.T.; Chen, W.T.; Hsu, Y.J.; Wei, K.H.; Lin, T.Y.; Lin, T.W. Interfacial Charge Carrier Dynamics in Core-Shell Au-CdS Nanocrystals. *J. Phys. Chem. C* **2010**, *114*, 11414–11420. [CrossRef]
33. Chen, F.; Zhao, J.; Hidaka, H. Highly selective deethylation of rhodamine B: Adsorption and photooxidation pathways of the dye on the TiO_2/SiO_2 composite photocatalyst. *Int. J. Photoenergy* **2003**, *5*, 209–217. [CrossRef]
34. Chen, D.; Yoo, S.H.; Huang, Q.; Ali, G.; Cho, S.O. Sonochemical Synthesis of Ag/AgCl Nanocubes and Their Efficient Visible-Light-Driven Photocatalytic Performance. *Chem. Eur. J.* **2012**, *18*, 5192–5200. [CrossRef]
35. Zhuang, J.; Dai, W.; Tian, Q.; Li, Z.; Xie, L.; Wang, J.; Liu, P. Photocatalytic Degradation of RhB over TiO_2 Bilayer Films: Effect of Defects and Their Location. *Langmuir* **2010**, *26*, 9686–9694. [CrossRef]
36. Yu, K.; Yang, S.; He, H.; Sun, C.; Gu, C.; Ju, Y. Visible Light-Driven Photocatalytic Degradation of Rhodamine B over $NaBiO_3$: Pathways and Mechanism. *J. Phys. Chem. A* **2009**, *113*, 10024–10032. [CrossRef]
37. Xu, H.; Li, H.; Xia, J.; Yin, S.; Luo, Z.; Liu, L.; Xu, L. One-Pot Synthesis of Visible-Light-Driven Plasmonic Photocatalyst Ag/AgCl in Ionic Liquid. *ACS Appl. Mater. Interfaces* **2011**, *3*, 22–29. [CrossRef]
38. Chen, C.; Zhao, W.; Li, J.; Zhao, J.; Hidaka, H.; Serpone, N. Formation and identification of intermediates in the visible-light-assisted photodegradation of sulforhodamine-B dye in aqueous TiO_2 dispersion. *J. Environ. Sci. Technol.* **2002**, *36*, 3604–3611. [CrossRef]
39. Huang, Y.; Li, J.; Ma, W.; Cheng, M.; Zhao, J. Efficient H_2O_2 Oxidation of Organic Pollutants Catalyzed by Supported Iron Sulfophenylporphyrin under Visible Light Irradiation. *J. Phys. Chem. B* **2004**, *108*, 7263–7270. [CrossRef]
40. Fu, H.; Pan, C.; Yao, W.; Zhu, Y. Visible-Light-Induced Degradation of Rhodamine B by Nanosized Bi_2WO_6. *J. Phys. Chem. B* **2005**, *109*, 22432–22439. [CrossRef]
41. Wang, P.; Cheng, M.; Zhang, Z. On different photodecomposition behaviors of rhodamine B on laponite and montmorillonite clay under visible light irradiation. *J. Saudi Chem. Soc.* **2014**, *18*, 308–316. [CrossRef]
42. Zhang, S.; Li, J.; Wang, X.; Huang, Y.; Zeng, M.; Xu, J. In Situ Ion Exchange Synthesis of Strongly Coupled Ag@AgCl/g-C_3N_4 Porous Nanosheets as Plasmonic Photocatalyst for Highly Efficient Visible-Light Photocatalysis. *ACS Appl. Mater. Interfaces* **2014**, *6*, 22116–22125. [CrossRef]
43. Xu, S.-M.; Pan, T.; Dou, Y.-B.; Yan, H.; Zhang, S.-T.; Ning, F.-Y.; Shi, W.-Y.; Wei, M. Theoretical and Experimental Study on $M^{II}M^{III}$-Layered Double Hydroxides as Efficient Photocatalysts toward Oxygen Evolution from Water. *J. Phys. Chem. C* **2015**, *119*, 18823–18834. [CrossRef]

44. Linic, S.; Christopher, P.B.; Ingram, D. Plasmonic-metal nanostructures for efficient conversion of solar to chemical energy. *Nat. Mater.* **2011**, *10*, 911–921. [CrossRef]
45. Wang, P.; Huang, B.; Qin, X.; Zhang, X.; Dai, Y.; Wei, J.; Whangbo, M.H. Ag@AgCl: A Highly Efficient and Stable Photocatalyst Active under Visible Light. *Angew. Chem. Int. Ed.* **2008**, *47*, 7931–7933. [CrossRef]
46. Zhang, H.; Fan, X.; Quan, X.; Chen, S.; Yu, H. Graphene Sheets Grafted Ag@AgCl Hybrid with Enhanced Plasmonic Photocatalytic Activity under Visible Light. *Environ. Sci. Technol.* **2011**, *45*, 5731–5736. [CrossRef]
47. Glaus, S.; Calzaferri, G. The band structures of the silver halides AgF, AgCl, and AgBr: A comparative study. *Photochem. Photobiol. Sci.* **2003**, *2*, 398–401. [CrossRef]
48. Zhou, Z.; Long, M.; Cai, W.; Cai, J. Synthesis and photocatalytic performance of the efficient visible light photocatalyst Ag–AgCl/$BiVO_4$. *J. Mol. Catal. A Chem.* **2012**, *353*, 22–28. [CrossRef]
49. Rai, M.; Yadav, A.; Gade, A. Silver nanoparticles as a new generation of antimicrobials. *Biotechnol. Adv.* **2009**, *27*, 76–83. [CrossRef]
50. He, W.; Kim, H.K.; Wamer, W.G.; Melka, D.; Callahan, J.H.; Yin, J.J. Photogenerated Charge Carriers and Reactive Oxygen Species in ZnO/Au Hybrid Nanostructures with Enhanced Photocatalytic and Antibacterial Activity. *J. Am. Chem. Soc.* **2014**, *136*, 750–757. [CrossRef]
51. Mao, C.; Xiang, Y.; Liu, X.; Cui, Z.; Yang, X.; Yeung, K.W.K.; Pan, H.; Wang, X.; Chu, P.K.; Wu, S. Photo-Inspired Antibacterial Activity and Wound Healing Acceleration by Hydrogel Embedded with Ag/Ag@AgCl/ZnO Nanostructures. *ACS Nano* **2017**, *11*, 9010–9021. [CrossRef]
52. Costantino, U.; Marmottini, F.; Nocchetti, M.; Vivani, R. New Synthetic Routes to Hydrotalcite-Like Compounds—Characterization and Properties of the Obtained Materials. *Eur. J. Inorg. Chem.* **1998**, *10*, 1439–1446. [CrossRef]